Direct numerical simulations of multi-mode immiscible Rayleigh-Taylor instability with high Reynolds numbers (EP)

Hong Liang (梁宏), Xiaoliang Hu (胡晓亮), Xuefeng Huang (黄雪峰), and Jiangrong Xu (徐江荣)

COLLECTIONS

(EP) This paper was selected as an Editor's Pick

View Online   Export Citation   CrossMark

AIP Author Services
English Language Editing

AIP
Publishing

Direct numerical simulations of multi-mode immiscible Rayleigh-Taylor instability with high Reynolds numbers ⓔⓟ

View Online   Export Citation   CrossMark

Hong Liang (梁宏),[a] **Xiaoliang Hu (胡晓亮), Xuefeng Huang (黄雪峰), and Jiangrong Xu (徐江荣)**[a]

AFFILIATIONS

Department of Physics, Hangzhou Dianzi University, Hangzhou 310018, China

[a]Authors to whom correspondence should be addressed: lianghongstefanie@163.com and jrxu@hdu.edu.cn

ABSTRACT

In this paper, we conduct the high-resolution direct numerical simulations of multimode immiscible Rayleigh-Taylor instability (RTI) with a low Atwood number ($A_t = 0.1$) using an improved phase field lattice Boltzmann method. The effect of the Reynolds number on the evolutional interfacial dynamics and bubble/spike amplitudes is first investigated by considering its wide range, from 100 up to a high value of 30 000. The numerical results show that, for sufficiently large Reynolds numbers, a sequence of distinguishing stages in the immiscible RTI can be observed, which includes the linear growth, saturated velocity growth, and chaotic development stages. At the late stage, the RTI induces a complex topology structure of the interface and a mass of dissociative drops can be significantly observed in the system. The accelerations of the bubble and spike front are also measured, and it is reported that their normalized values at the late time are, respectively, approximate to the constant values of around 0.025 and 0.027, exhibiting a terminally quadratic growth. As the Reynolds number is reduced to small ones, the multiple disturbances of the RTI are found to merge into a larger one at the initial stage. Then, the evolutional interfaces display the patterns familiar from the single-mode RTI. The phase interfaces in the whole process become very smooth without the appearance of the breakup phenomenon, and the spike and bubble velocities at the late time approach constant values. Furthermore, we also analyze the effects of the initial conditions in terms of the perturbation wavelength and amplitude, and it is found that the instability undergoes a faster growth at the intermediate stage for a larger wavelength, while the late-time bubble and spike growth rates are insensitive to the changes of the initially perturbed wavelength and amplitude.

Published under license by AIP Publishing. https://doi.org/10.1063/1.5127888

I. INTRODUCTION

The Rayleigh-Taylor instability (RTI) occurs when a heavier fluid sits atop a lighter fluid with a perturbed interface subject to a gravitational field. The RTI is a very classic and basic interfacial instability and has long been of interest to fluid researchers because of its great importance and relevance to many scientific and engineering applications, such as inertial confinement fusion, astrophysics, and meteorology.[1–5] The pioneering exploration of the RTI problem was attributed to Rayleigh[6] and Taylor,[7] who put forward the classical linear stability theory and found that the amplitude of the perturbation has an initial exponential growth. In their analysis, the viscosities of binary fluids and the surface tension force between them have been neglected. Following their strategy, the effects of the viscosity, surface tension force, and compressibility on the

development of the RTI were analyzed and the modified linear growth theories including these physical factors were proposed in succession.[8–10] The early investigations of the RTI mainly concentrated on the case with a single-mode initial perturbation not only because it is the most simple and fundamental instability phenomenon but also because the turbulent growth constant in the multimode RTI depends critically on the knowledge of single-mode terminal velocity. Sharp[11] provided a good summary on the early studies of the RTI and reported that the development of the instability can be roughly divided into four stages. In the first stage, the linear theory is used to describe the growth of the initial perturbation until reaching the amplitude of $0.1\lambda - 0.4\lambda$, where λ is the wavelength. This is followed by the second stage, where the amplitude of the perturbation grows nonlinearly to a size of about λ, and the spike and bubble structures

are formed. During the third stage, the nonlinear effect becomes increasingly significant and the spike rolls up at its tail end, leading to the formation of a mushroomlike pattern. Finally, the breakup of the spike can be induced by various mechanisms and the turbulent or chaotic mixing of the fluids dominates the fourth stage. Following the work of Sharp,[11] numerous researchers have extensively investigated the single-mode RTI in the regimes of the nonlinear and chaotic mixing by using the experimental,[12–14] theoretical,[15–17] and numerical[18–27] approaches. Our recent lattice Boltzmann simulations[23,25] of the single-mode RTI have also confirmed that the instability would undergo four distinguishing stages at high Reynolds numbers known as the linear growth, terminal velocity growth, reacceleration, and chaotic development stages. The spike and bubble velocities at the second stage agree well with the solutions of the classical potential flow theory,[15] and the late-time growth of the bubble exhibits a mean quadratic law.

Alternatively, the RTI with a multimode initial perturbation has become an increasingly important subject since it is more omnipresent in nature and practical engineering applications compared to the ideal single-mode example. Due to its importance, the multimode RTI has nourished the enthusiasm of many mathematicians and scientists, while to the best of our knowledge, the majority of the research studies just focus on the multimode instability between two miscible fluids[28–44] and relatively little attention has been paid to the multimode RTI of immiscible fluids. The miscible and immiscible RTIs behave differently in that the diffusion effect exists in the former event and the surface tension force between miscible fluids is also absent. It has been commonly accepted that the diffusion reduces the growth rate of the instability.[45,46] Besides, the evolution of immiscible RTI with the surface tension exhibits a variety of interesting behaviors such as capillary waves, pinching, and breakup.[47] Youngs[48,49] performed the early numerical simulation using the interface tracking method and experimental study to investigate the multimode immiscible RTI with various density ratios. Their experimental results have confirmed the mixing patterns induced by the instability in the simulations. Glimm *et al.*[50] also utilized the interface tracking method to simulate the multimode immiscible RTI of binary compressible fluids and reported that their numerical results were in quantitative agreement with the laboratory experiment under the approximately incompressible condition. Dimonte and Schneider[51] experimentally examined the effect of the temporal acceleration profile on the development of the multimode immiscible RTI with a fixed density ratio and found that the turbulent mixing strongly depends on the temporal acceleration. For the constant acceleration, the bubble amplitude grows with the familiar quadratic law, while it is described by a new formula for the temporal acceleration. The density ratio dependence of Rayleigh-Taylor mixing under the temporal acceleration profile was also studied experimentally in their later work.[52] Schneider *et al.*[53] used the experiment to study the multimode RTI of two immiscible fluids at a high Reynolds number and showed that the measured growth rate for the bubble is consistent with the previous experiment[51] but is narrower than the model prediction[54] due to the appearance of the internal structures in the bubble. Clark[55] used a lattice Boltzmann multiphase model to simulate the multimode immiscible RTI and discussed the effect of the initial condition. He found that a small variation in the initial condition yields a large variation in the growth rate, and to achieve the self-similarity result, a statistical

basis for measuring the growth rate was provided. The dependency of the multimode RTI growth rate on the initial condition was also analyzed in subsequent work.[56] Several researchers[47,57,58] have investigated the effect of the surface tension force on the evolution of the multimode immiscible RTI with mild Reynolds numbers and reported that the instability in the presence of the surface tension could generate some fascinating interfacial phenomena.

As reviewed above, there have been some works on the multimode immiscible RTI, which can provide good insights into the understanding of this complex instability phenomenon. However, a majority of these works only focus on the cases with the small or moderate Reynolds numbers and the time duration of the instability is relatively short. In this paper, we invoke an improved phase field lattice Boltzmann method[23] to numerically study the late-time dynamics of the multimode immiscible RTI. The effects of the wide Reynolds numbers, the initial conditions in terms of the perturbation wavelength and amplitude on the interfacial behaviors, and bubble and spike evolutional amplitudes and velocities are investigated in detail. The rest of this paper is organized as follows: In Sec. II, we give a brief introduction of the adopted numerical method. Then the method is validated in Sec. III by simulating the classical single-mode RTI. Section IV describes the longtime evolution of multimode instability within a comprehensive range of physical quantities. Finally, we conclude with a summary in Sec. V.

II. MATHEMATICAL METHOD

The phase-field method[59] has become increasingly popular for simulating multiphase flows owing to its firm physics in interface capturing. In the method, an order parameter is introduced to distinguish different phases, and the phase interface is treated as a transition region with finite thickness across which the physical quantities of fluids are allowed to change smoothly. From different angles of view, two kinds of interface capturing equations in the phase-field method are commonly used: the Cahn-Hilliard equation[60,61] and the Allen-Cahn equation.[62,63] In the former equation, the diffusive flow rate is taken to be proportional to the gradient of the chemical potential, and it can conserve the total mass of system with the appropriate boundary conditions. The Cahn-Hilliard equation has been used to simulate many complex multiphase flow systems, such as phase separation, viscoelastic multiphase flow, interfacial instability, moving contact line, and so on. In this regard, the classical Cahn-Hilliard equation used for the interface capturing can be expressed by[23,60]

$$\frac{\partial \phi}{\partial t} + \nabla \cdot (\phi \mathbf{u}) = \nabla \cdot M(\nabla \mu), \tag{1}$$

where ϕ is the order parameter taking 0 and 1 in the bulk regions, and the interface position is marked by the contour level of $\phi = 0.5$, M is the mobility coefficient, $\mathbf{u}$ is the fluid velocity, and μ is the chemical potential given by

$$\mu = 4\beta\phi(\phi - 1)(\phi - 0.5) - k\nabla^2\phi, \tag{2}$$

where the physical parameters k and β are determined by the interface thickness (D) and the surface tension (σ),

$$k = \frac{3}{2}\sigma D, \quad \beta = \frac{12\sigma}{D}. \tag{3}$$

The flow is calculated by the incompressible Navier-Stokes equations, including the surface tension and external forces,

$$\nabla \cdot \mathbf{u} = 0, \tag{4a}$$

$$\frac{\partial \rho \mathbf{u}}{\partial t} + \nabla \cdot (\rho \mathbf{u}\mathbf{u}) = -\nabla p + \nabla \cdot \left[\nu \rho (\nabla \mathbf{u} + \nabla \mathbf{u}^T) \right] + \mathbf{F}_s + \mathbf{G}, \tag{4b}$$

where ρ is the density, p is the hydrodynamic pressure, ν is the kinematic viscosity, $\mathbf{G}$ is the external force, and $\mathbf{F}_s$ is the surface tension force, which is computed by

$$\mathbf{F}_s = \mu \nabla \phi. \tag{5}$$

In addition to defining the phase interface, the order parameter is also used to smooth the density jump across the interface according to the following formula:

$$\rho = \phi(\rho_l - \rho_g) + \rho_g, \tag{6}$$

where ρ_l and ρ_g are the densities of the liquid and gas phases, respectively.

Based on the kinetic theory, the mesoscopic lattice Boltzmann method has developed into a powerful numerical tool for simulating complex flow systems, in particular, multiphase flows.[64] Several multiphase lattice Boltzmann models have been proposed from different physical pictures of the intermolecular interactions, among which the phase field type of lattice Boltzmann model[23,62] has received great attention because of its advantages such as low spurious velocity and high numerical accuracy in interface tracking. In the current work, an improved lattice Boltzmann method[23] will be adopted to solve the coupled Cahn-Hilliard and Navier-Stokes equation systems. The method utilizes two evolution equations, which can be

written as

$$f_i(\mathbf{x} + \mathbf{c}_i \delta_t, t + \delta_t) - f_i(\mathbf{x}, t) = -\frac{1}{\tau_f} \left[f_i(\mathbf{x}, t) - f_i^{eq}(\mathbf{x}, t) \right] + \delta_t F_i(\mathbf{x}, t), \tag{7}$$

$$g_i(\mathbf{x} + \mathbf{c}_i \delta_t, t + \delta_t) - g_i(\mathbf{x}, t) = -\frac{1}{\tau_g} \left[g_i(\mathbf{x}, t) - g_i^{eq}(\mathbf{x}, t) \right] + \delta_t G_i(\mathbf{x}, t), \tag{8}$$

where $f_i(\mathbf{x}, t)$, $g_i(\mathbf{x}, t)$ are the particle distribution functions, $f_i^{eq}(\mathbf{x}, t)$ and $g_i^{eq}(\mathbf{x}, t)$ are the corresponding equilibrium distribution functions, τ_f and τ_g are the relaxation factors, and F_i and G_i are the forcing distribution functions. To recover the target equations exactly, the equilibrium distribution functions f_i^{eq}, g_i^{eq} should be defined as[23]

$$f_i^{eq} = \begin{cases} \phi + (\omega_i - 1)\eta\mu, & i = 0, \\ \omega_i \eta \mu + \omega_i \phi \frac{\mathbf{c}_i \cdot \mathbf{u}}{c_s^2}, & i \neq 0 \end{cases} \tag{9}$$

and

$$g_i^{eq} = \begin{cases} \frac{p}{c_s^2}(\omega_i - 1) + \rho s_i(\mathbf{u}), & i = 0, \\ \frac{p}{c_s^2}\omega_i + \rho s_i(\mathbf{u}), & i \neq 0 \end{cases} \tag{10}$$

with

$$s_i(\mathbf{u}) = \omega_i \left[\frac{\mathbf{c}_i \cdot \mathbf{u}}{c_s^2} + \frac{(\mathbf{c}_i \cdot \mathbf{u})^2}{2c_s^4} - \frac{\mathbf{u} \cdot \mathbf{u}}{2c_s^2} \right], \tag{11}$$

where c_s is the sound speed, η is a parameter used to adjust the mobility, $\mathbf{c}_i$ are the discrete velocities, and ω_i are the weighting coefficients. For the two-dimensional flows, we adopt the popular D2Q9 lattice model[65–67] in which the weighting coefficients ω_i are given by $\omega_0 = 4/9$, $\omega_{1-4} = 1/9$, $\omega_{5-8} = 1/36$ and the discrete velocities $\mathbf{c}_i$ can be expressed by

$$\mathbf{c}_i = \begin{cases} (0,0)c, & i = 0, \\ (\cos[(i-1)\pi/2], \sin[(i-1)\pi/2])c, & i = 1-4, \\ \sqrt{2}(\cos[(i-5)\pi/2 + \pi/4], \sin[(i-5)\pi/2 + \pi/4])c, & i = 5-8. \end{cases} \tag{12}$$

To be consistent with the governing equation, a source term should be introduced in the LB equation (7) and is designed as[23]

$$F_i = \left(1 - \frac{1}{2\tau_f}\right) \frac{\omega_i \mathbf{c}_i \cdot \partial_t(\phi \mathbf{u})}{c_s^2}. \tag{13}$$

Besides, the discrete lattice effects should also be considered in the incorporation of a force into the lattice Boltzmann approach. In this work, a simplified forcing distribution function is proposed,[62]

$$G_i = \left(1 - \frac{1}{2\tau_g}\right) \omega_i \left[\frac{\mathbf{c}_i \cdot (\mathbf{F}_s + \mathbf{G})}{c_s^2} + \frac{\mathbf{u}\nabla\rho : \mathbf{c}_i \mathbf{c}_i}{c_s^2} \right]. \tag{14}$$

Taking the zeroth- or first-order moment of the distribution functions f_i, g_i, the macroscopic quantities ϕ, $\mathbf{u}$, and p can be explicitly computed by

$$\phi = \sum_i f_i, \tag{15a}$$

$$\rho \mathbf{u} = \sum_i \mathbf{c}_i g_i + 0.5\delta_t(\mathbf{F}_s + \mathbf{G}), \tag{15b}$$

$$p = \frac{c_s^2}{(1 - \omega_0)} \left[\sum_{i \neq 0} g_i + \frac{\delta_t}{2} \mathbf{u} \cdot \nabla\rho + \rho s_0(\mathbf{u}) \right]. \tag{15c}$$

With the Chapman-Enskog technique,[23,62] we can show that the used lattice Boltzmann method can correctly recover the Navier-Stokes and Cahn-Hilliard coupled equations in which the viscosity and mobility can be determined by

$$\nu = c_s^2(\tau_g - 0.5)\delta_t, \tag{16a}$$

$$M = \eta c_s^2(\tau_f - 0.5)\delta_t. \tag{16b}$$

In practice, the temporal derivative in the model is computed by the explicit Euler difference scheme, i.e., $\partial_t(\phi \mathbf{u}) = [\phi(t)\mathbf{u}(t) - \phi(t - \delta_t)\mathbf{u}(t - \delta_t)]/\delta_t$, and the following isotropic central

difference schemes are used to estimate the spacing derivatives of the order parameter:

$$\nabla\phi(\mathbf{x}) = \sum_{i\neq 0} \frac{\omega_i \mathbf{c}_i \phi(\mathbf{x} + \mathbf{c}_i \delta t)}{c_s^2 \delta_t}, \tag{17}$$

$$\nabla^2 \phi(\mathbf{x}) = \sum_{i\neq 0} \frac{2\omega_i[\phi(\mathbf{x} + \mathbf{c}_i \delta t) - \phi(\mathbf{x})]}{c_s^2 \delta_t^2}, \tag{18}$$

which can be further used to determine the gradient of the fluid density by the relation $\nabla\rho = (\rho_l - \rho_g)\nabla\phi$.

III. METHOD VALIDATION

Before we proceed any further, we first conducted a typical simulation of single-mode RTI to validate the used numerical method and compared the numerical results with the literature data.[60] The simulation was carried out in a computational domain of $\left[-\frac{W}{2}, \frac{W}{2}\right] \times [-2W, 2W]$, where a heavier fluid seated on the top of a lighter fluid under a gravitational field. The initial interface of binary fluids was imposed by a small perturbation with a cosine function of $0.1W \cos(2\pi x/W)$. The RTI problem can be described by two dimensionless physical quantities, i.e., the Reynolds number (Re) and the Atwood number (A_t) defined by

$$Re = \frac{W\sqrt{gW}}{\nu}, \quad A_t = \frac{\rho_l - \rho_g}{\rho_l + \rho_g}, \tag{19}$$

where g is the gravitational acceleration. To incorporate the gravitational effect, the following body force $\mathbf{G}$ is imposed on two fluids:

$$\mathbf{G} = \left[0, \ -\left(\rho - \frac{\rho_l + \rho_g}{2}\right)g\right]. \tag{20}$$

As used in Ref. 60, the simulated Atwood and Reynolds numbers are set as 0.5 and 3000, respectively. Some other physical parameters in the simulation are given as $W = 200$, $\rho_g = 1$, $D = 4$, $\tau_f = 0.8$, and $\sigma = 10^{-5}$, and the Peclet number defined by $Pe = \sqrt{gW}D/M\beta$

is fixed as 420. Here, we set the characteristic length equal to $W = 200$ and the characteristic time $T = \sqrt{W/gA_t} = 10^4$. Figure 1(a) depicts the snapshots of the interface patterns at the dimensionless times $\tau = 1$, 1.5, 2, and 2.5. It can be found that under the action of the gravity, the heavy and light fluids penetrate into each other with time, which then leads to the formation of the spike and bubble. The spike increases in size, accompanied by its roll-up at the end due to the Kelvin-Helmholtz instability. As a result, a fascinating structure of two counter-rotating vortices is generated in the system. The two vortices further develop and a pair of secondary vortices appear at the tails of the roll-ups. The evolutional patterns of the phase interface obtained by the present method compare well with the previous literature results.[60] Furthermore, we also conducted a quantitative comparison between the lattice Boltzmann simulation results and the finite-volume solutions[60] in terms of the bubble and spike positions. It is shown in Fig. 1(b) that the present numerical predictions agree well with the previous solutions using the finite-volume scheme,[60] which demonstrates that the lattice Boltzmann method attains enough precision in simulating the RTI problem.

IV. NUMERICAL RESULTS AND DISCUSSIONS

The physical system studied in this work consists of a two-dimensional rectangular pipe, which is discretized by a fine mesh of $L \times W = 2000 \times 1000$. Initially, a heavy fluid lies above a light fluid with a multimode random perturbation on the phase interface,

$$h(x) = 0.5L + A_m W \sum_{n=30}^{40} \left[a_n \cos\left(\frac{2\pi n}{\lambda}x\right) + b_n \sin\left(\frac{2\pi n}{\lambda}x\right)\right], \tag{21}$$

where A_m is a positive coefficient that determines the initial amplitude of the perturbation, λ is the wavelength, and a_n, b_n are chosen from a Gaussian random distribution on the interval, $-1 < a_n, b_n < 1$. To be smooth across the interface, the initial distribution for the order parameter can be given by
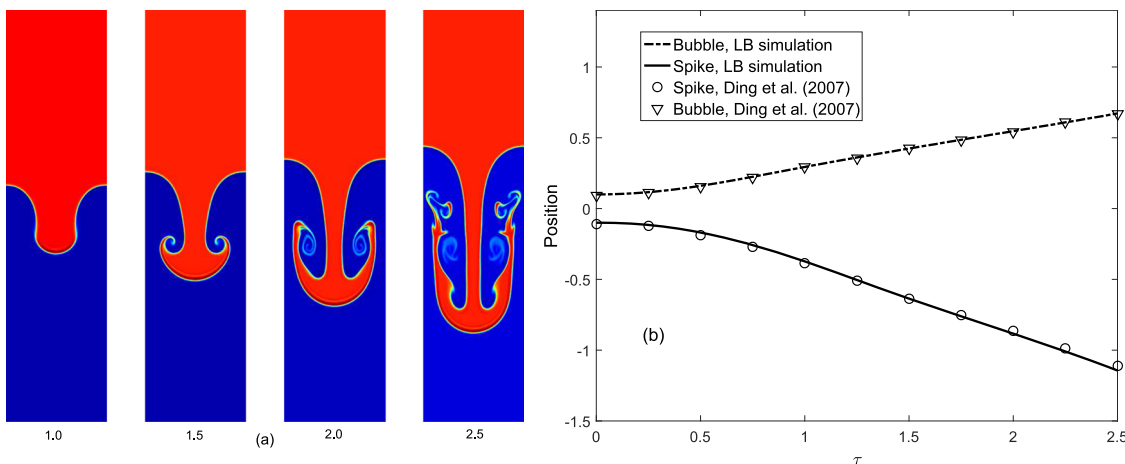

FIG. 1. (a) Snapshots of the interface patterns and (b) time evolutions of the bubble and spike positions in the single-mode RTI with $Re = 3000$ and $A_t = 0.5$.

$$\phi(x,y) = 0.5 + 0.5 \tanh \frac{2[y - h(x)]}{D}, \tag{22}$$

where D is the interface thickness fixed to be four lattice units. The top and bottom boundaries are the solid walls treated by the no-slip bounce back boundary conditions, and the periodic boundary conditions are applied in the left and right boundaries. In the simulations, the densities of liquid (ρ_l) and gas (ρ_g) fluids are set to be $\frac{11}{9}$ and 1, corresponding to a low Atwood number of 0.1, and some physical parameters are configured as $U_0 = \sqrt{gW} = 0.1$, $\tau_f = 0.8$, and $Pe = 50$. We choose the parameters W, U_0, and W/U_0 as the characteristic length, velocity, and time, and it should be noted that the statistical quantities presented below have been normalized by these characteristic values. For the convenience of the discussions, we also give an illustration on the statistical method of the used physical quantities. The bubble and spike positions are defined by the lowest and highest points of the phase interfaces in the vertical direction. The statistic spike and bubble amplitudes marked by h_s, h_b are measured by the y-directional maximum distances between the spike/bubble fronts and their initial positions. The spike and bubble velocities denoted by u_s, u_b can be computed from the amplitude profiles by the time derivatives of h_s, h_b. The following method proposed by Clark[55] is used for measuring the spike and bubble growth rate coefficients, which exhibits a better convergence property,

$$\alpha_{b,s} = \frac{\partial h_{b,s}}{\partial Z} = \frac{\partial h_{b,s}}{\partial z}\frac{\partial z}{\partial Z} = \frac{1}{2A_t}\frac{\partial h_{b,s}}{\partial z}, \tag{23}$$

where $Z = 2A_t z$, $z = gt^2/2$, and t is the time that the acceleration is applied.

A. Effect of the Reynolds number

The effect of the Reynolds number is first investigated by adjusting the fluid viscosity. The surface tension is set as an ultralow value of 5×10^{-5} to mimic the experimental circumstances,[53,68] where the liquid surfactant was added at the interface to reduce the surface tension between the fluids. Besides, the initial conditions in terms of the coefficient A_m and the wavelength λ are given as 0.002 and W. Figure 2 depicts the time evolutions of the interfacial patterns in the multimode RTI with a comprehensive range of Reynolds numbers. These patterns are included to give a qualitative impression of the two-dimensional character of this instability. It can be found from Fig. 2 that the fluid interface displays the distinct behaviours at different Reynolds numbers. For high Reynolds numbers, the heavy fluid initially falls down and the light fluid rises up under the influence of the gravitational force, namely, they penetrate into each other, which develops into some slender spikes and small bubbles. The formed spikes and bubbles continue to grow in a fairly independent fashion, which leads to the formation of a mushroomlike structure similar to the experimental observation of miscible RTI.[32] Then, the modes begin to couple to one another and some of the spikes roll up at their tails due to the appearance of the Kelvin-Helmholtz instabilities,[69] which indicates that the instability has been transformed into the nonlinear regime. The Kelvin-Helmholtz instability can effectively promote the mixing of two fluids. As time progresses, the interaction among the modes becomes more and more intensive, and this increasingly nonlinear coupling of the modes reflected in the merging of bubbles and spikes induce

the formation of the large-scale interface structures. Finally, the large scales in the system continue to increase in size until the mixing layer becomes fully turbulent. Meanwhile, the close inspection shows that some small-scale dissociative drops can also be generated in the mixing layer. The range of scale structures appeared in the flows at a very high Reynolds number conform to the classical Kolmogorov turbulence theory[70] in which the kinetic energy in the flows is first injected into the large-scale vortex structure that can be successively disintegrated into some small-scale vortices. This transfer of the kinetic energy from the large-scale to small-scale structures cannot last indefinitely. When the vortex structure is small enough, the viscosity of the fluid will dominate, and the kinetic energy converted into internal energy dissipation will not pass to the smaller scales. Besides, we also would like to point out that the evolutional interface patterns in the immiscible RTI obtained by the present numerical simulation are qualitatively consistent with those of the previous experimental studies.[52,53] As the Reynolds number is reduced to a moderate value, we can find from Fig. 2 that the development of the instability at the early stage is relatively slow. Some of the initial perturbations merge into the large ones that significantly reduce the number of the modes. Then, the newly formed modes continue to grow in size and the interaction between them compared to the former case is weak, although the roll-up phenomenon of the spikes can also be observed. In the following, the interaction among bubbles increases with time and the eventual chaotic mixing layer can also be visual in the system. As for a sufficiently low Reynolds number, it can be found from Fig. 2 that the multiple disturbances of the RTI merge into a larger one at the initial stage. This is because the hydrodynamic effect at this time is extremely weak and the dominated surface tension force makes the coalescence of these small disturbances. Then, the evolutional interfaces in the whole process display the patterns familiar from the single-mode RTI and no obvious vortices or interfacial breakup phenomenon at the late-time stage can be observed due to the stabilized shear layer between the high viscous bubbles and spikes.

We also conducted a quantitative investigation of the Reynolds number effect on the bubble and spike amplitudes and their evolutional velocities, which are the concerned physical quantities in the studies of RTI.[25,32,53] Figures 3(a) and 3(b) show the time variations of the normalized bubble amplitude and velocity in the multimode immiscible RTI with a comprehensive range of Reynolds numbers. It can be found from Figs. 3(a) and 3(b) that the bubble amplitude increases with time for all Reynolds numbers, while it achieves a greater value at a larger Re. The bubble velocity also shows an increase with the Reynolds number at the early stage, and it has a late-time oscillation with the time for the cases of high Reynolds numbers as similarly reported in the previous simulations of the single-mode RTI.[21,22,25] Nonetheless, a greater average velocity of the bubble at the late time can be attained for a larger Reynolds number. The analogical curves for describing the growth of the spike can also be found in Figs. 4(a) and 4(b), where the spike amplitude and its temporal velocity are presented. We now performed the theoretical analysis on the development of the multimode instability. The dynamics of the spike front in the incompressible RTI is governed by a balance per unit mass of the buoyant and dissipation forces as[46]

$$\frac{dh}{dt} = u, \qquad \frac{du}{dt} = \frac{\delta\rho}{\bar{\rho}}g + F_d, \tag{24}$$
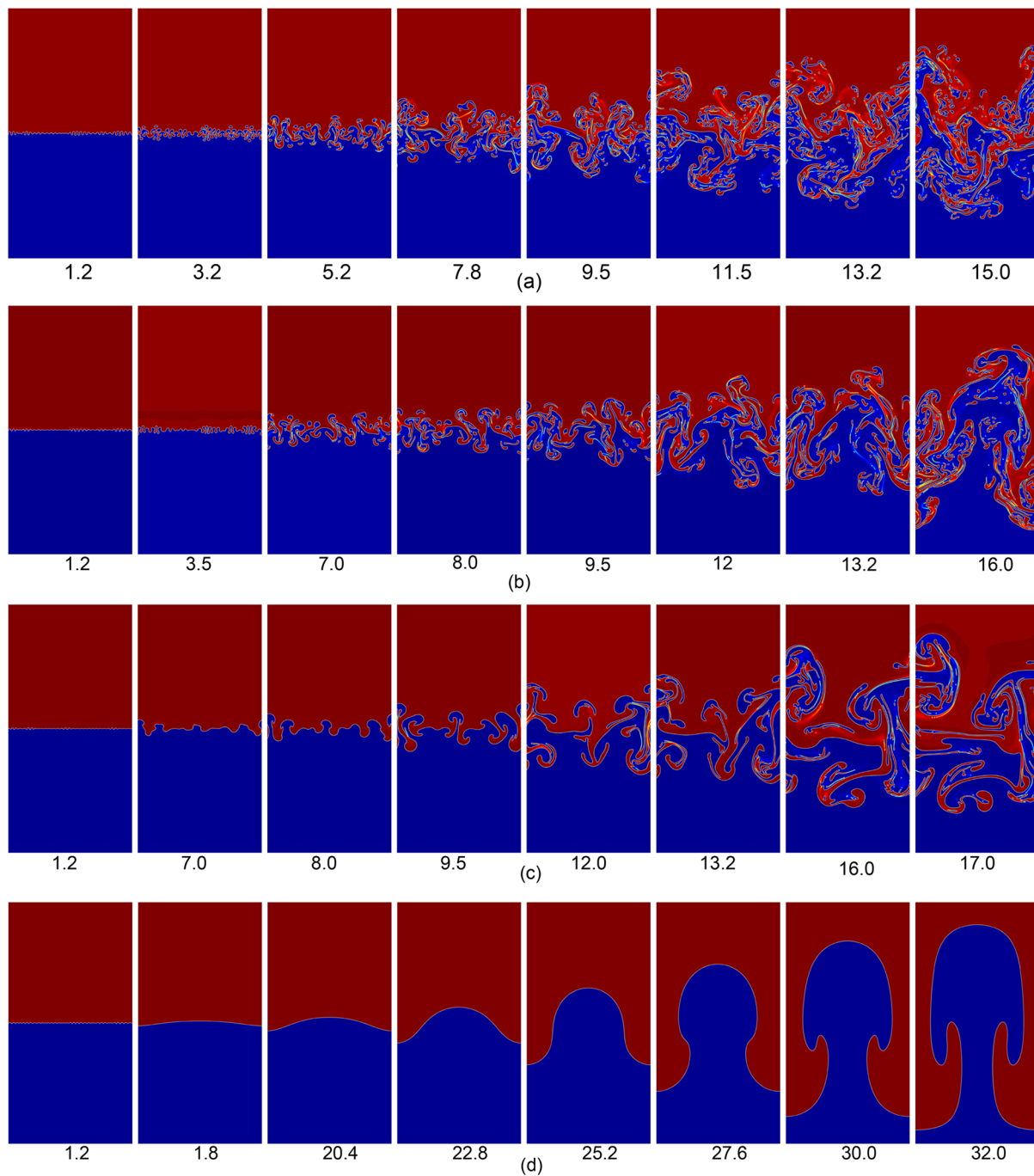
FIG. 2. The time evolutions of the interfacial patterns in the multimode immiscible RTI with different Reynolds numbers: (a) $Re = 30\,000$, (b) $Re = 10\,000$, (c) $Re = 3000$, and (d) $Re = 100$.

where h is the spike position, u is the velocity, $\delta\rho/\bar{\rho}$ is a function of the density ratio with the relations $\delta\rho = (\rho_l - \rho_g)/2$ and $\bar{\rho} = (\rho_l + \rho_g)/2$, and F_d is the dissipation force defined by the rate of momentum loss in the direction of gravity, $F_d = -\varepsilon/v$, where ε is the energy dissipation rate. On the other hand, Sreenivasan[71] suggested that the energy dissipation rate in the condition of no viscous time scale can be given as $\varepsilon = Cv^3/W$, where C is a constant. Substituting the formula into Eq. (24), one can find that a lower dissipation force
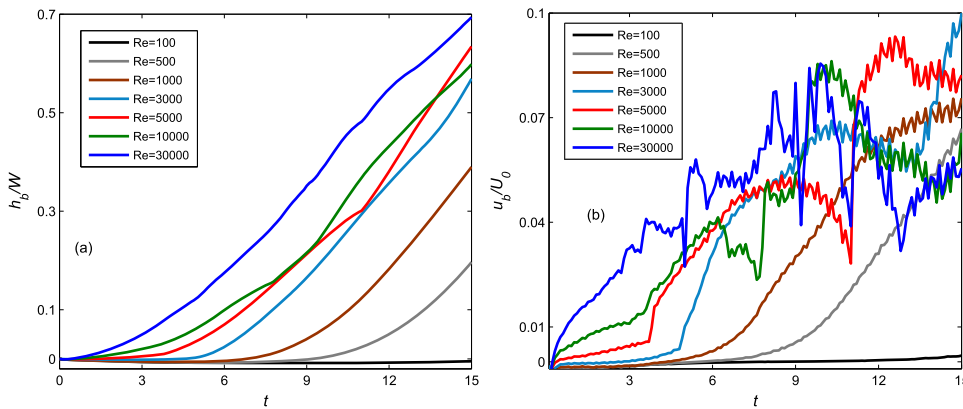
FIG. 3. Time variations of the (a) normalized bubble amplitude and (b) normalized bubble velocity in the multimode immiscible RTI with various Reynolds numbers.

accelerating the spike growth can be achieved in theory for a higher Reynolds number. This theoretical analysis can also be well confirmed in our present numerical simulations, where the fluid interface of the immiscible RTI indeed attains a larger growth velocity at a larger Reynolds number.

Furthermore, we examined the effect of the Reynolds number on the growth stages of the multimode immiscible RTI. For a high Reynolds number, we can divide the development of the multimode instability into three distinguishing stages. In the first stage, the perturbations grow with an exponential form according to the linear stability theory. Then, the bubbles and spikes are formed, which will evolve with a nearly constant velocity as shown in Figs. 3(b) and 4(b), indicating that the instability has entered into the second stage of the saturated velocity. The time duration of the second stage is relatively short in this case with a small wavelength, and the saturated velocity regime can be well identified in the multimode RTI with a long wavelength shown below. The bubble and spike velocities eventually become unstable and fluctuate with the time, which suggests that the instability has been transformed into the chaotic growth stage. The late-time growths for the spike and bubble have been the focus of the attention in the research of the multimode RTI,[30,34,35,40] and it has been widely recognized that their late-time evolutions can be characterized by a quadratic function of $h_{b,s} = \alpha_{b,s} A_t g t^2$. To determine the nature of the instability growth at the late stage, here we

also measured the bubble and spike growth rates α_b, α_s with the various Reynolds numbers and showed the results in Figs. 5(a) and 5(b). It can be found from Figs. 5(a) and 5(b) that for high Reynolds numbers, the bubble and spike growth rates at the late stage have some slight fluctuations, and their statistic average values approach to the constants of 0.025 and 0.027, respectively, indicating that the multimode immiscible RTI undergoes a mean quadratic growth. The predicted values for the bubble and spike growth rates are shown to fall into the region of 0.02–0.04 reported in the most of previous numerical simulations of miscible multimode RTI.[30,34,35] In addition, the growth of the bubble and spike fronts is nearly symmetric for a very small Atwood number, and Dimonte and Schneider[52] experimentally summarized a straightforward formula for describing the relationship between the spike and bubble growth rates, $\alpha_s = \alpha_b r^{D_\alpha}$, where $r = \rho_l/\rho_g$ is the density ratio and D_α is a constant value of 0.33 ± 0.05. We computed the value of D_α by the present simulation and found that the numerically predicted value is about 0.38, which shows a good agreement with the experimental result. As the Reynolds numbers are reduced to the small ones, it is found that the late-time chaotic development stage can be no longer attained.

B. Effect of the initial condition

The initial condition is an important physical quantity of the multimode RIT, and its effect has been extensively studied in the
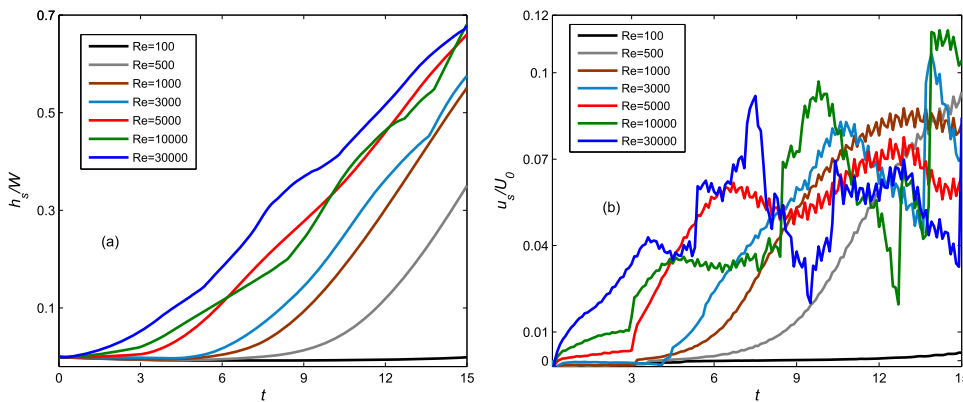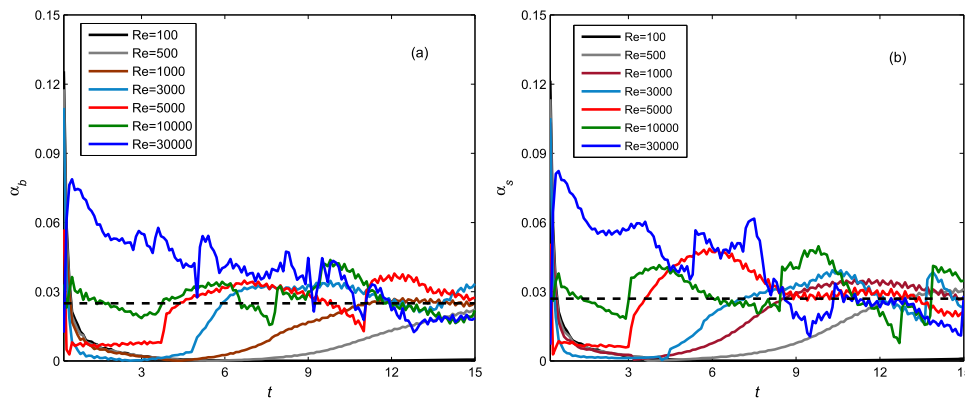

FIG. 4. Time variations of the (a) normalized spike amplitude and (b) normalized spike velocity in the multimode immiscible RTI with various Reynolds numbers.

FIG. 5. The effect of the Reynolds number on the growth rate coefficients of the (a) bubble and (b) spike fronts. The left and right dashed lines represent the constant values of 0.025 and 0.027.

miscible cases.[33,35,72–74] How the initial condition influences the development of the multimode immiscible RTI has not been fully discussed. To address this question, in this subsection, we will conduct a comprehensive study on the effect of the initial condition in terms of the perturbation wavelength and amplitude, which are two effective parameters to characterize the initial distribution of the immiscible instability. In the simulations, the Reynolds number is given as an ultrahigh value of 30 000, the initial amplitude parameter A_m is fixed as 0.002, and the remaining parameters are set to be those of Subsection IV A. We first consider the effect of the initially setting

wavelength, and the snapshots of the interfacial patterns in the multimode immiscible RTI with three typical wavelengths of $\lambda = W$, $3W$, $5W$ are plotted in Figs. 2(a) and 6. It can be found from Figs. 2(a) and 6 that the early-time growths of the perturbations show little dependence on the wavelength. For all cases, the perturbations initially grow in a fairly independent fashion until forming the spike and bubble structures. The spikes and bubbles continue to increase in size and then begin to couple to one another. As time goes on, the mushroomlike structure can be visible for all wavelengths. The increase in the wavelength can reduce the competition among the
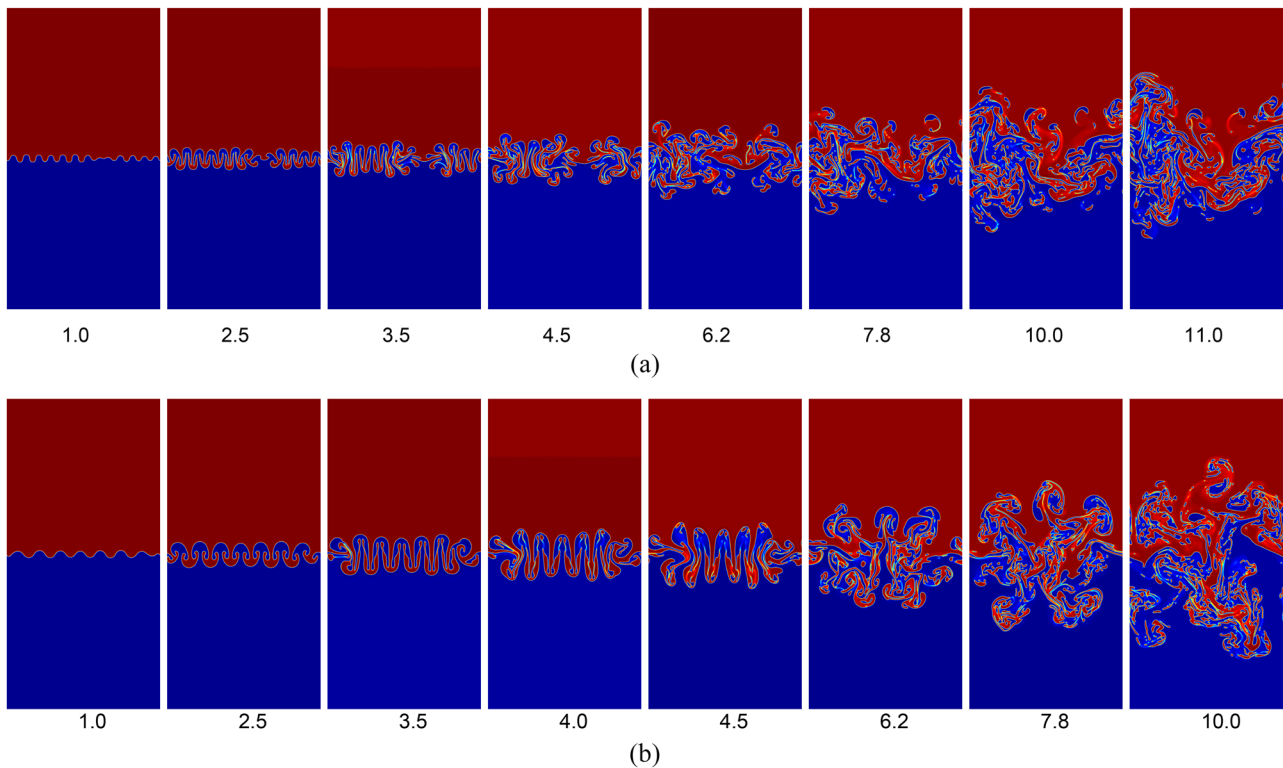

FIG. 6. The snapshots of the interfacial patterns in the multimode immiscible RTI with different wavelengths: (a) $\lambda = 3W$ and (b) $\lambda = 5W$.
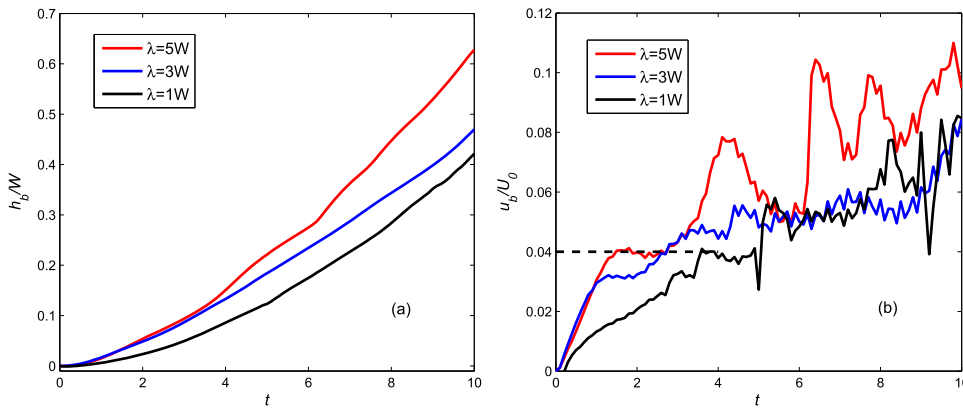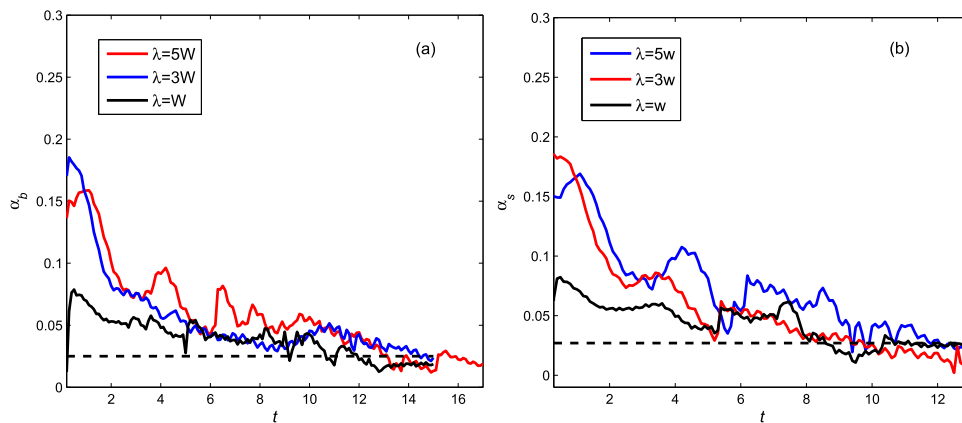
FIG. 7. Effect of the initial wavelength on the (a) normalized bubble amplitude and (b) normalized bubble velocity with a high Reynolds number of 30 000. The dashed line represents a constant of 0.04.

modes and the modes inside the mushroom can be more uniform. In the following, the interactions among the modes become more and more intensive, and some of the modes coalesce into the large ones. Meanwhile, some small-scale structures can also be produced inside the large-scale structures, which eventually induces the chaotic mixing of two fluids for all wavelengths. Besides, it is shown that the chaotic mixing appears at a shorter time for a smaller wavelength due to the increase in the mode number and the more complex and intensive interactions among these modes. To quantitatively show the effect of the wavelength, we also measured the time evolutions of the bubble and spike amplitudes and velocities and showed the results in Figs. 7 and 8. It can be found from Figs. 7 and 8 that the wavelength has no significant effect on the bubble and spike growths at the initial linear development stage. The initial curves for the bubble and spike amplitudes and velocities at different wavelengths match each other. After that, the wavelength starts to affect the instability development, and it is shown that the spike and bubble enable to obtain greater amplitudes and evolutional velocities for a larger wavelength, which is attributed to the relenting interactions among the modes promoting the y-directional movements of the spike and bubble. In this case, the spike and bubble reach the saturated velocities within a shorter time, and their normalized velocity values approach to 0.042 and 0.04, which are found to be insensitive with the change of the wavelength. At the late time, the

spike and bubble velocities regardless of the wavelength are unstable and fluctuate with time, while higher averaging velocities of the bubble and spike can be achieved for a larger wavelength. Furthermore, we also investigated the effect of the initial wavelength on the bubble and spike growth rates, which are the most concerned quantities in the study of the multimode RTI. The time evolutions of the bubble and spike normalized accelerations with three different wavelengths are plotted in Figs. 9(a) and 9(b), where the computational mesh in the vertical direction for the cases of $\lambda = 3W, 5W$ has been increased to 3000 for a longer evolutional time. It can be seen from Figs. 9(a) and 9(b) that increasing the wavelength enables to improve the bubble and spike normalized accelerations at the intermediate stage, while the eventual bubble and spike growth rates at the late-time stage approach to the constant values, which are further found to be almost independent of the initial wavelength. This indicates that the flow has lost the memory of the initial condition and eventually exhibits the self-similarity chaotic mixing features. The self-similarity phenomenology was also reported in the previous studies of the multimode RTI[11,48,49] but was discrepant with the recent numerical simulations of miscible case,[33,72,74] where the instability within the presence of initial long wavelengths causes the accelerations of the late-time bubble and spike growth rates. This discrepancy may be attributed to that the Reynolds numbers they considered are relatively small and the durations of the instability
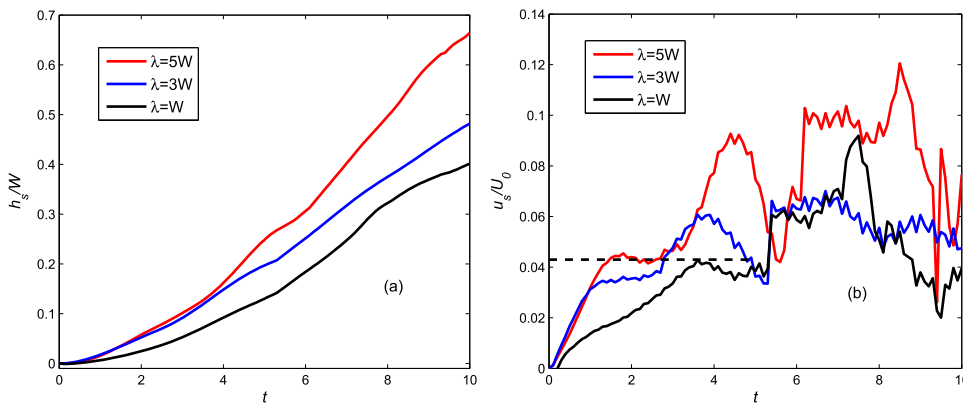
FIG. 8. Effect of the initial wavelength on the (a) normalized spike amplitude and (b) normalized spike velocity with a high Reynolds number of 30 000. The dashed line represents a constant of 0.042.

FIG. 9. Effect of the initial wavelength on the (a) normalized bubble acceleration and (b) normalized spike acceleration at a high Reynolds number of 30 000. The dashed lines in (a) and (b) mark the constant values of 0.025 and 0.027, respectively.

are also short. Actually, we indeed observe from Figs. 9(a) and 9(b) that increasing the initial wavelength can improve the bubble and spike growth rates at some stages, while they eventually decrease to the similar saturated values at the late time.

Furthermore, we investigated the effect of the perturbation amplitude on the development of the immiscible multimode RTI. In the following studies, an ultrahigh Reynolds number of 30 000 is considered, the surface tension is given as $\sigma = 5 \times 10^{-5}$, and the initial wavelength is fixed as W. The snapshots of the interfacial patterns in the multimode immiscible RTI with three different perturbation amplitudes are plotted in Figs. 2(a) and 10. We can roughly observe from Figs. 2(a) and 10 that the interfaces display the similar dynamic behaviours that are insensitive to the initial perturbation amplitudes. The heavy and light fluids initially penetrate into each other and form spikes and bubbles. The spike and bubble continue to develop into a mushroomlike structure, although the modes in the structure are not uniform and slightly disordered due to the larger competition in the presence of the initial short wavelength. As time
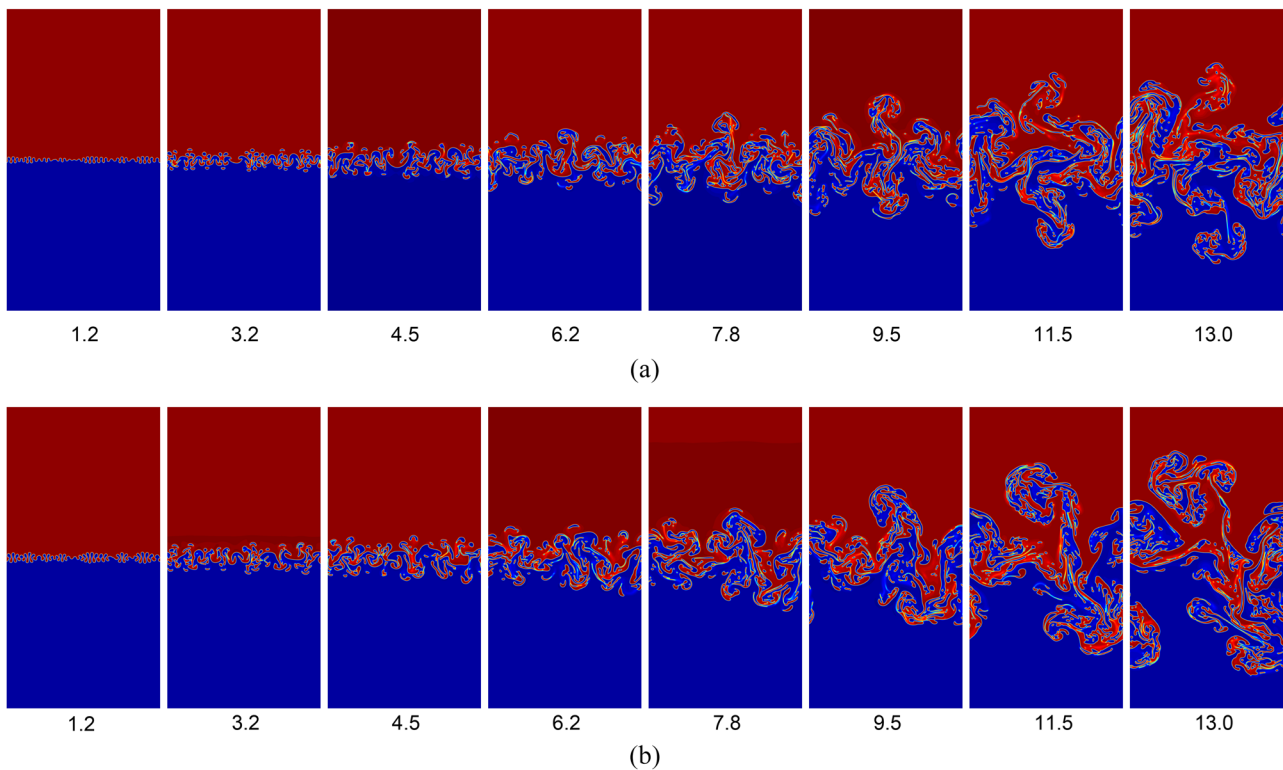
FIG. 10. The snapshots of the interfacial patterns in the multimode immiscible RTI with different perturbation amplitudes: (a) $A_m = 0.003$ and (b) $A_m = 0.006$.
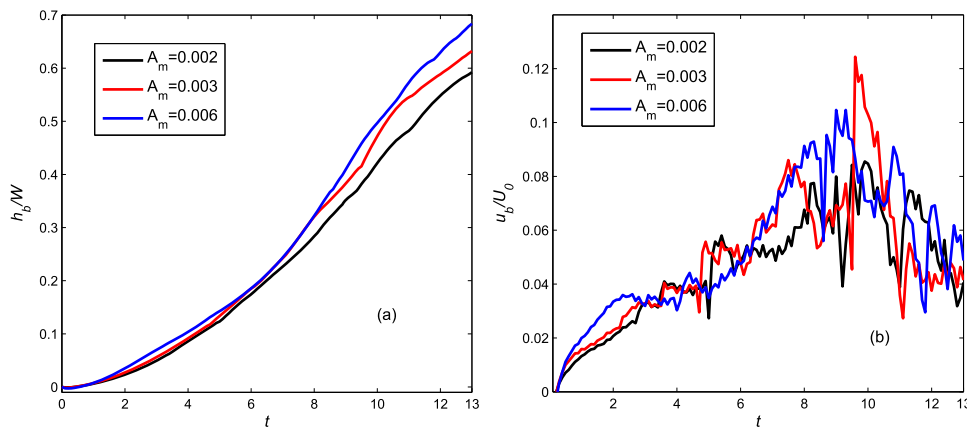
FIG. 11. Effect of the initial perturbation amplitude on the evolutional (a) bubble amplitude and (b) bubble velocity at a high Reynolds number of 30 000.

goes on, the nonlinear effect becomes more and more intensive. The interfaces undergo a dramatic deformation and some of them even have a chaotic breakup, which ultimately induces the formation of numerous small dissociative drops in the system. The effect of the initial perturbation amplitude on the bubble and spike evolutional amplitudes and velocities is also examined, and we presented the dimensionless results in Figs. 11 and 12. It can be found from Figs. 11 and 12 that the amplitude change does not induce substantial changes in the evolutions of the bubble and spike amplitude at

the linear and saturated velocity stages, while the close inspection shows that the slightly greater values for the bubble and spike amplitudes can be achieved at a larger initial perturbation amplitude. This trend can be obviously observed when the instability evolves into the late-time stage and becomes completely turbulent. Nonetheless, the effect of the initial perturbation amplitude on the bubble and spike evolutional amplitudes is weak in general. The little influence of the initial amplitude is also shown in the evolutional curves for the bubble and spike velocities. In addition, the bubble and spike
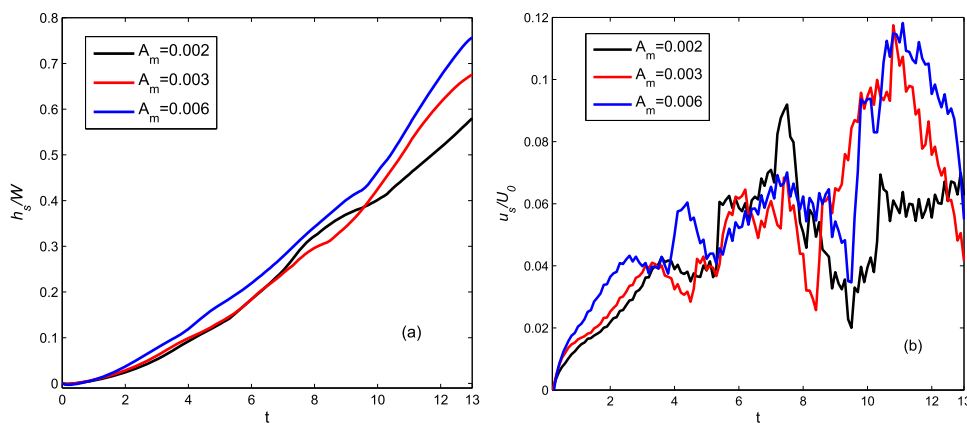

FIG. 12. Effect of the initial perturbation amplitude on the evolutional (a) spike amplitude and (b) spike velocity at a high Reynolds number of 30 000.
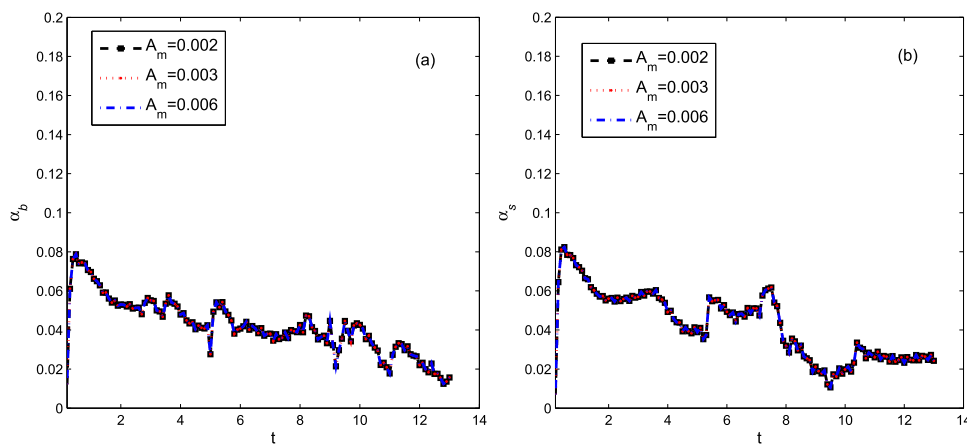

FIG. 13. Effect of the initial perturbation amplitude on the (a) bubble normalized acceleration and (b) spike normalized acceleration at a high Reynolds number.

late-time growth rates are the most important parameters in the understanding of the multimode RTI and we further test the effect of the perturbation amplitude on them. Figure 13 shows the time evolutions of the normalized bubble and spike accelerations at three different perturbation amplitudes. It can be observed that the change in perturbation amplitude does not cause any fluctuation in the bubble and spike growth factors, and three curves perfectly coincide with each other. This indicates that the flow has lost the memory of the initial condition in terms of the perturbation amplitude and the instability at the late-time stage exhibits the self-similarity feature. The present results are consistent with the previous research of miscible multimode RTI,[75] where it is reported that the bubble growth rate is insensitive to the initial amplitude.

V. CONCLUSIONS

In this paper, the multimode immiscible RTI with a low Atwood number of 0.1 is systematically studied using an advanced phase-field lattice Boltzmann method. The effects of several important physical quantities, including the Reynolds number, and the initial conditions are investigated in detail. The high-resolution numerical simulations show that the multimode instability displays distinct interfacial dynamics at different Reynolds numbers. For high Reynolds numbers, the development of the multimode immiscible RTI can be summarized into three stages, including the linear growth, saturated velocity growth, and chaotic development stages. At the second stage, a very fascinating mushroomlike structure is successfully reproduced. Then, the modes start to couple to one another and the interactions among them increase in time. The increasingly nonlinear coupling of the modes reflects the merging of small-scale structures into large-scale ones. The large scales continue to develop in size with the appearance of the interfacial breakup, and the turbulent or chaotic mixing of the fluids dominates the eventual stage of the instability, where numerous small dissociative drops are also induced. To show the late-time growth nature of the multimode RTI, we further measured the bubble and spike acceleration and reported that their dimensionless growth rates approach the constant values of 0.025 and 0.027, respectively, indicating a late-time quadratic growth law. For a very small Reynolds number, it is found that the multiple perturbations merge into a larger one at the initial stage, and the following development of the instability displays the interfacial patterns familiar from the single-mode RTI. The evolutional phase interfaces in the whole process become very smooth and the late-time chaotic mixing stage cannot be reached. In addition, we also studied the effect of the initial conditions on the instability development in terms of the initial perturbation wavelength and amplitude. It is found that the late-time bubble and spike growth rates are almost insensitive with the initial conditions, which implies that the flow has the memory of the initial conditions, and the multimode immiscible RTI exhibits the self-similarity chaotic mixing growth. Finally, we would like to point out that the present investigation only focused on the incompressible RTI under the isothermal circumstance. The two-phase RTI within the thermal system surely exhibits both the hydrodynamic nonequilibrium behaviors and the thermodynamic nonequilibrium effects, which have been attracting more investigations by the discrete Boltzmann model.[24,26,27,76,77] This interesting subject could constitute one of our future works.

REFERENCES

[1] A. Burrows, "Supernova explosions in the universe," Nature **403**, 727–733 (2000).

[2] Y. Zhou, "Rayleigh-Taylor and Richtmyer-Meshkov instability induced flow, turbulence, and mixing. I," Phys. Rep. **720-722**, 1–136 (2017).

[3] Y. Zhou, "Rayleigh-Taylor and Richtmyer-Meshkov instability induced flow, turbulence, and mixing. II," Phys. Rep. **723-725**, 1–160 (2017).

[4] G. Boffetta and A. Mazzino, "Incompressible Rayleigh-Taylor turbulence," Annu. Rev. Fluid Mech. **49**, 119–143 (2017).

[5] J. X. Chen, Y. G. Chen, and R. Kapral, "Chemically propelled motors navigate chemical patterns," Adv. Sci. **5**, 1800028 (2018).

[6] Lord Rayleigh, "Investigation of the character of the equilibrium of an incompressible heavy fluid of variable density," Proc. London Math. Soc. **14**, 170–177 (1883).

[7] G. I. Taylor, "The instability of liquid surfaces when accelerated in a direction perpendicular to their plane," Proc. R. Soc. London, Ser. A **201**, 192 (1950).

[8] S. Chandrasekhar, *Hydrodynamic and Hydromagnetic Stability* (Oxford University Press, Oxford, 1961).

[9] M. Mitchner and R. K. M. Landshoff, "Rayleigh-Taylor instability for compressible fluids," Phys. Fluids **7**, 862 (1964).

[10] R. Menikoff, R. C. Mjolsness, D. H. Sharp, and C. Zemach, "Unstable normal mode for Rayleigh-Taylor instability in viscous fluids," Phys. Fluids **20**, 2000 (1977).

[11] D. H. Sharp, "An overview of Rayleigh-Taylor instability," Physica D **12**, 3 (1984).

[12] J. T. Waddell, C. E. Niederhaus, and J. W. Jacobs, "Experimental study of Rayleigh-Taylor instability: Low Atwood number liquid systems with single-mode initial perturbations," Phys. Fluids **13**, 1263 (2001).

[13] J. P. Wilkinson and J. W. Jacobs, "Experimental study of the single-mode three-dimensional Rayleigh-Taylor instability," Phys. Fluids **19**, 124102 (2007).

[14] J. White, J. Oakley, M. Anderson, and R. Bonazza, "Experimental measurements of the nonlinear Rayleigh-Taylor instability using a magnetorheological fluid," Phys. Rev. E **81**, 026303 (2010).

[15] V. N. Goncharov, "Analytical model of nonlinear, single-mode, classical Rayleigh-Taylor instability at arbitrary Atwood numbers," Phys. Rev. Lett. **88**, 134502 (2002).

[16] R. Betti and J. Sanz, "Bubble acceleration in the ablative Rayleigh-Taylor instability," Phys. Rev. Lett. **97**, 205002 (2006).

[17] S. I. Sohn, "Effects of surface tension and viscosity on the growth rates of Rayleigh-Taylor and Richtmyer-Meshkov instabilities," Phys. Rev. E **80**, 055302(R) (2009).

[18] G. Tryggvason, "Numerical simulations of the Rayleigh-Taylor instability," J. Comput. Phys. **75**, 253–282 (1988).

[19] X. Y. He, R. Y. Zhang, S. Y. Chen, and G. D. Doolen, "On the three-dimensional Rayleigh-Taylor instability," Phys. Fluids **11**, 1143 (1999).

[20] A. Celani, A. Mazzino, P. M. Ginanneschi, and L. Vozella, "Phase-field model for the Rayleigh-Taylor instability of immiscible fluids," J. Fluid Mech. **622**, 115–134 (2009).

[21] P. Ramaprabhu, G. Dimonte, P. Woodward, C. Fryer, G. Rochefeller, K. Muthuraman, P.-H. Lin, and J. Jayaraj, "The late-time dynamics of the single-mode Rayleigh-Taylor instability," Phys. Fluids **24**, 074107 (2012).

[22] T. Wei and D. Livescu, "Late-time quadratic growth in single-mode Rayleigh-Taylor instability," Phys. Rev. E **86**, 046405 (2012).

[23] H. Liang, B. C. Shi, Z. L. Guo, and Z. H. Chai, "Phase-field-based multiple-relaxation-time lattice Boltzmann model for incompressible multiphase flows," Phys. Rev. E **89**, 053320 (2014).

[24]H. L. Lai, A. G. Xu, G. C. Zhang, Y. B. Gan, Y. J. Ying, and S. Succi, "Nonequilibrium thermohydrodynamic effects on the Rayleigh-Taylor instability in compressible flows," Phys. Rev. E **94**, 023106 (2016).

[25]H. Liang, Q. X. Li, B. C. Shi, and Z. H. Chai, "Lattice Boltzmann simulation of three-dimensional Rayleigh-Taylor instability," Phys. Rev. E **93**, 033113 (2016).

[26]C. D. Lin, A. G. Xu, G. C. Zhang, K. H. Luo, and Y. J. Li, "Discrete Boltzmann modeling of Rayleigh-Taylor instability in two-component compressible flows," Phys. Rev. E **96**, 053305 (2017).

[27]F. Chen, A. G. Xu, and G. C. Zhang, "Collaboration and competition between Richtmyer-Meshkov instability and Rayleigh-Taylor instability," Phys. Fluids **30**, 102105 (2018).

[28]S. B. Dalziel, P. F. Linden, and D. L. Youngs, "Self-similarity and internal structure of turbulence induced by Rayleigh-Taylor instability," J. Fluid Mech. **399**, 1–48 (1999).

[29]Y. N. Young, H. Tufo, A. Dubey, and R. Rosner, "On the miscible Rayleigh-Taylor instability: Two and three dimensions," J. Fluid Mech. **447**, 377–408 (2001).

[30]A. W. Cook and P. E. Dimotakis, "Transition stages of Rayleigh-Taylor instability between miscible fluids," J. Fluid Mech. **443**, 69–99 (2001).

[31]P. Ramaprabhu and M. J. Andrews, "Experimental investigation of Rayleigh-Taylor mixing at small Atwood numbers," J. Fluid Mech. **502**, 233–271 (2004).

[32]A. W. Cook, W. Cabot, and P. L. Miller, "The mixing transition in Rayleigh-Taylor instability," J. Fluid Mech. **511**, 333–362 (2004).

[33]P. Ramaprabhu, G. Dimonte, and M. J. Andrews, "A numerical study of the influence of initial perturbations on the turbulent Rayleigh-Taylor instability," J. Fluid Mech. **536**, 285–319 (2005).

[34]W. H. Cabot and A. W. Cook, "Reynolds number effects on Rayleigh-Taylor instability with possible implications for type Ia supernovae," Nat. Phys. **2**, 562–568 (2006).

[35]A. Banerjee and M. J. Andrews, "3D simulations to investigate initial condition effects on the growth of Rayleigh-Taylor mixing," Int. J. Heat Mass Transfer **52**, 3906–3917 (2009).

[36]D. H. Olson and J. W. Jacobs, "Experimental study of Rayleigh-Taylor instability with a complex initial perturbation," Phys. Fluids **21**, 034103 (2009).

[37]H. Lim, J. Iwerks, J. Glimma, and D. H. Sharp, "Nonideal Rayleigh-Taylor mixing," Proc. Natl. Acad. Sci. U. S. A. **107**, 12786–12792 (2010).

[38]G. C. Burton, "Study of ultrahigh Atwood-number Rayleigh-Taylor mixing dynamics using the nonlinear large-eddy simulation method," Phys. Fluids **23**, 045106 (2011).

[39]D. Livescu, "Numerical simulations of two-fluid turbulent mixing at large density ratios and applications to the Rayleigh-Taylor instability," Philos. Trans. R. Soc., A Trans. R. Soc. A **371**, 20120185 (2013).

[40]B. Akula and D. Ranjan, "Dynamics of buoyancy-driven flows at moderately high Atwood numbers," J. Fluid Mech. **795**, 315–355 (2016).

[41]Y. K. Wei, Z. D. Wang, H. S. Dou, and Y. H. Qian, "A novel two-dimensional coupled lattice Boltzmann model for incompressible flow in application of turbulence Rayleigh-Taylor instability," Comput. Fluids **156**, 97–102 (2017).

[42]L. Biferale, G. Boffetta, A. A. Mailybaev, and A. Scagliarini, "Rayleigh-Taylor turbulence with singular nonuniform initial conditions," Phys. Rev. Fluids **3**, 092601(R) (2018).

[43]Y. K. Wei, H. Yang, Z. Lin, Z. D. Wang, and Y. H. Qian, "A novel two-dimensional coupled lattice Boltzmann model for thermal incompressible flows," Appl. Math. Comput. **339**, 556–567 (2018).

[44]Y. Zhou and W. H. Cabot, "Time-dependent study of anisotropy in Rayleigh-Taylor instability induced turbulent flows with a variety of density ratios," Phys. Fluids **31**, 084106 (2019).

[45]J. Glimm, J. W. Grove, X. L. Li, W. Oh, and D. H. Sharp, "A critical analysis of Rayleigh-Taylor growth rates," J. Comput. Phys. **169**, 652–677 (2001).

[46]S. I. Abarzhi, A. Gorobets, and K. R. Sreenivasan, "Rayleigh-Taylor turbulent mixing of immiscible, miscible and stratified fluids," Phys. Fluids **17**, 081705 (2005).

[47]S. I. Sohn and S. Baek, "Bubble merger and scaling law of the Rayleigh-Taylor instability with surface tension," Phys. Lett. A **381**, 3812–3817 (2017).

[48]D. L. Youngs, "Numerical simulation of turbulent mixing by Rayleigh-Taylor instability," Physica D **12**, 32–44 (1984).

[49]D. L. Youngs, "Modelling turbulent mixing by Rayleigh-Taylor instability," Physica D **37**, 270–287 (1989).

[50]J. Glimm, X. L. Li, R. Menikoff, D. H. Sharp, and Q. Zhang, "A numerical study of bubble interactions in Rayleigh-Taylor instability for compressible fluids," Phys. Fluids A **2**, 2046–2054 (1990).

[51]G. Dimonte and M. Schneider, "Turbulent Rayleigh-Taylor instability experiments with variable acceleration," Phys. Rev. E **54**, 3740–3743 (1996).

[52]G. Dimonte and M. Schneider, "Density ratio dependence of Rayleigh-Taylor mixing for sustained and impulsive acceleration histories," Phys. Fluids **12**, 304–321 (2000).

[53]M. B. Schneider, G. Dimonte, and B. Remington, "Large and small scale structure in Rayleigh-Taylor mixing," Phys. Rev. Lett. **80**, 3507–3510 (1998).

[54]U. Alon, J. Hecht, D. Ofer, and D. Shvarts, "Power laws and similarity of Rayleigh-Taylor and Richtmyer-Meshkov mixing fronts at all density ratios," Phys. Rev. Lett. **74**, 534–537 (1995).

[55]T. T. Clark, "A numerical study of the statistics of a two-dimensional Rayleigh-Taylor mixing layer," Phys. Fluids **15**, 2413–2423 (2003).

[56]G. Dimonte, "Dependence of turbulent Rayleigh-Taylor instability on initial perturbations," Phys. Rev. E **69**, 056305 (2004).

[57]M. Chertkov, I. Kolokolov, and V. Lebedev, "Effects of surface tension on immiscible Rayleigh-Taylor turbulence," Phys. Rev. E **71**, 055301(R) (2005).

[58]Y. N. Young and F. E. Ham, "Surface tension in incompressible Rayleigh-Taylor mixing flow," J. Turbul. **7**, 1–23 (2006).

[59]D. Jacqmin, "Calculation of two-phase Navier-Stokes flows using phase-field modeling," J. Comput. Phys. **155**, 96–127 (1999).

[60]H. Ding, P. D. M. Spelt, and C. Shu, "Diffuse interface model for incompressible two-phase flows with large density ratios," J. Comput. Phys. **226**, 2078–2095 (2007).

[61]H. Liang, J. R. Xu, J. X. Chen, H. L. Wang, Z. H. Chai, and B. C. Shi, "Phase-field-based lattice Boltzmann modeling of large-density-ratio two-phase flows," Phys. Rev. E **97**, 033309 (2018).

[62]H. Liang, H. H. Liu, Z. H. Chai, and B. C. Shi, "Lattice Boltzmann method for contact-line motion of binary fluids with high density ratio," Phys. Rev. E **99**, 063306 (2019).

[63]H. Liang, Y. Li, J. X. Chen, and J. R. Xu, "Axisymmetric lattice Boltzmann model for multiphase flows with large density ratio," Int. J. Heat Mass Transfer **130**, 1189–1205 (2019).

[64]Z. L. Guo and C. Shu, *Lattice Boltzmann Method and Its Applications in Engineering* (World Scientific, Singapore, 2013).

[65]Y. K. Wei, Z. D. Wang, J. F. Yang, H. S. Dou, and Y. H. Qian, "A simple lattice Boltzmann model for turbulence Rayleigh-Benard thermal convection," Comput. Fluids **118**, 167–171 (2015).

[66]Y. K. Wei, Z. D. Wang, H. S. Dou, Y. H. Qian, and W. W. Yan, "Simulation of natural convection heat transfer in an enclosure at different Rayleigh number using lattice Boltzmann method," Comput. Fluids **124**, 30–38 (2016).

[67]Y. K. Wei, Z. D. Wang, and Y. H. Qian, "A numerical study on entropy generation in two-dimensional Rayleigh-Benard convection at different Prandtl number," Entropy **19**, 433-01–433-13 (2017).

[68]Z. Huang, A. D. Luca, T. J. Atherton, M. Bird, C. Rosenblatt, and P. Carles, "Rayleigh-Taylor instability experiments with precise and arbitrary control of the initial interface shape," Phys. Rev. Lett. **99**, 204502 (2007).

[69]Y. B. Gan, A. G. Xu, G. C. Zhang, and Y. J. Li, "Lattice Boltzmann study on Kelvin-Helmholtz instability: Roles of velocity and density gradients," Phys. Rev. E **83**, 056704 (2011).

[70]A. N. Kolmogorov, "The local structure of turbulence in incompressible viscous fluid for very large Reynolds numbers," Dokl. Akad. Nauk SSSR **30**, 301–305 (1941).

[71]K. R. Sreenivasan, "On the scaling of the turbulence energy dissipation rate," Phys. Fluids **27**, 1048 (1984).

[72]P. Ramaprabhu and M. J. Andrews, "On the initialization of Rayleigh-Taylor simulations," Phys. Fluids **16**, L59–L62 (2004).

[73]N. J. Mueschke and O. Schilling, "Investigation of Rayleigh-Taylor turbulence and mixing using direct numerical simulation with experimentally measured

initial conditions. I. Comparison to experimental data," Phys. Fluids **21**, 014106 (2009).

[74]N. J. Mueschke and O. Schilling, "Investigation of Rayleigh-Taylor turbulence and mixing using direct numerical simulation with experimentally measured initial conditions. II. Dynamics of transitional flow and mixing statistics," Phys. Fluids **21**, 014107 (2009).

[75]G. Dimonte, D. L. Youngs, A. Dimits, S. Weber, M. Marinak *et al.*, "A comparative study of the turbulent Rayleigh-Taylor instability using high-resolution three-dimensional numerical simulations: The Alpha-Group collaboration," Phys. Fluids **16**, 1668–1693 (2004).

[76]F. Chen, A. G. Xu, and G. C. Zhang, "Viscosity, heat conductivity, and Prandtl number effects in the Rayleigh-Taylor instability," Front. Phys. **11**, 114703 (2016).

[77]D. M. Li, H. L. Lai, A. G. Xu, G. C. Zhang, C. D. Lin, and Y. B. Gan, "Discrete Boltzmann simulation of Rayleigh-Taylor instability in compressible flows," Acta Phys. Sin. **67**, 080501 (2018).